

Stellar and Dynamical Masses of Ellipticals in the Sloan Digital Sky Survey

Nikhil Padmanabhan¹*, Uroš Seljak¹, Michael A. Strauss², Michael R. Blanton³, Guinevere Kauffmann⁴, David J. Schlegel², Christy Tremonti⁵, Neta A. Bahcall², Mariangela Bernardi⁶, J. Brinkmann⁷, Masataka Fukugita⁸, Željko Ivezić²

¹Joseph Henry Laboratories, Jadwin Hall, Princeton University, Princeton, NJ 08544

²Dept. of Astrophysical Sciences, Peyton Hall, Princeton University, Princeton, NJ 08544

³Dept. of Physics, NYU, 4 Washington Place, New York, NY 10003

⁴Max Planck Institut für Astrophysik, Karl-Schwarzschild-Str. 1, D-85741 Garching, Germany

⁵Steward Observatory, 933 N Cherry Ave., Tucson AZ 85721-0065

⁶Department of Physics, Carnegie Mellon University, 5000 Forbes Avenue, Pittsburgh, PA 15213

⁷Apache Point Observatory, P.O.Box 59, Sunspot, NM 88349-0059

⁸Institute for Cosmic-Ray Research, University of Tokyo, Kashiwa 277-8582, Japan

23 September 2018

ABSTRACT

We study the variation of the dark matter mass fraction of elliptical galaxies as a function of their luminosity, stellar mass, and size using a sample of 29,469 elliptical galaxies culled from the Sloan Digital Sky Survey. We model ellipticals as a stellar Hernquist profile embedded in an adiabatically compressed dark matter halo. This model allows us to estimate a dynamical mass (M_{dynm}) at the half-light radius from the velocity dispersion of the spectra, and to compare these to the stellar mass estimates (M_*) from Kauffmann et al. (2003). We find that M_*/L is independent of luminosity, while M_{dynm}/L increases with luminosity, implying that the dark matter fraction increases with luminosity. We also observe that at a fixed luminosity or stellar mass, the dark matter fraction increases with increasing galaxy size or, equivalently, increases with decreasing surface brightness: high surface brightness galaxies show almost no evidence for dark matter, while in low surface brightness galaxies, the dark matter exceeds the stellar mass at the half light radius. We relate this to the fundamental plane of elliptical galaxies, suggesting that the tilt of this plane from simple virial predictions is due to the dark matter in galaxies. We find that a simple model where galaxies are embedded in dark matter halos and have a star formation efficiency independent of their surface brightness explains these trends. We estimate the virial mass of ellipticals as being approximately 7–30 times their stellar mass, with the lower limit suggesting almost all of the gas within the virial radius is converted into stars.

1 INTRODUCTION

The zoo of galaxies is an eclectic one, with large variations in morphologies, colours and spectra. This is perhaps not very surprising, given the varied environments in which galaxies reside and the different processes underlying their formation. However, a number of regular trends are also known; for instance, the rotation velocities of spiral galaxies and the central velocity dispersions of elliptical galaxies correlate strongly with luminosity – the Tully & Fisher (1977) and Faber & Jackson (1976) relations. In addition, elliptical galaxies appear to reside in a thin plane in the space of their luminosity (L), radius (R), and central velocity dispersion (σ), the “fundamental plane” (Djorgovski & Davis 1987; Dressler et al. 1987), of which the Faber-Jackson relation is a projection. Understanding the source of these

regularities is still an open problem; they provide a strong constraint and challenge to theories of galaxy formation.

Elliptical galaxies are probably the simplest galaxies to model. These are pressure supported systems, and are remarkably uniform in their properties. Their intensity profiles are well described by a de Vaucouleurs (1948) profile, $I \propto \exp(-(\theta/\theta_s)^{1/4})$, they have very simple spectral energy distributions and they have very uniform photometric properties. However, very little has been known about the matter content of elliptical galaxies until recently, principally due to the lack of dynamical tracers like the HI rotation curves for spiral galaxies. More recently however, there have been a number of surveys that have measured the dynamical structure of samples of elliptical galaxies using slit spectroscopy (Kronawitter et al. 2000), and with the advent of integral field spectroscopy (de Zeeuw et al. 2002), the num-

ber of well studied elliptical galaxies will only increase. In addition, strong lensing measurements (eg. Koopmans & Treu 2003) have added independent measures of the masses of the halos of ellipticals, especially at radii outside the realm of spectroscopic techniques.

The Sloan Digital Sky Survey (SDSS, York et al. 2000) presents a different model for studying elliptical galaxies. Unlike the surveys above that collect very detailed dynamical information for a small number of galaxies, the SDSS, with its π steradians of deep multicolour imaging and 10^6 spectra, will measure global parameters for a very large number of galaxies, allowing one to statistically approach questions of galaxy structure. Indeed, the properties of elliptical galaxies in the SDSS have already been studied in great detail (Bernardi et al 2003a, 2003b, 2003c, 2003d). This work constructed a sample of 9000 galaxies from early SDSS data, and exhaustively measured the various correlations between different observables. Principal results include a Faber-Jackson relation between luminosity L and velocity dispersion σ , $\sigma \propto L^{0.25 \pm 0.012}$, and a fundamental plane relation between the effective radius R , the half-light surface brightness I , and σ , $R \propto \sigma^{1.49 \pm 0.05} I^{-0.75 \pm 0.01}$. This statistical approach has been further extended using the weak lensing information from galaxy-galaxy lensing at large radii (McKay et al. 2001) and models satisfying the dynamical constraints from velocity dispersions and weak lensing in an average sense have been constructed (Seljak 2002).

This paper explores the dark matter content of elliptical galaxies in the SDSS in more detail. Is there evidence for dark matter in ellipticals? How does it correlate with the luminosity and size of the galaxy? How does the dynamical mass compare to the stellar mass of elliptical galaxies? The simplest virial prediction combined with a constant mass to light ratio implies that $L \propto \sigma^2 R$; however, the observed fundamental plane (FP) of ellipticals shows the scaling $L \propto \sigma^{1.98} R^{0.66}$ (Bernardi et al. 2003c). There have been a number of proposals in the literature to explain this deviation from the virial prediction, or ‘tilt’. Implicit in the virial prediction is the assumption that elliptical galaxies form a homologous sequence, i.e. the dynamical structure of elliptical galaxies are self similar and related by simple scaling relations. Deviations from such a sequence would naturally manifest themselves as a tilt in the FP. However, based on detailed dynamical measurements of nearby ellipticals, Gerhard et al. (2001) argue that there is little evidence for any deviations from homology. A second, and preferred, proposal is to assume that M/L is not constant, but varies with luminosity. Such a variation could be caused either due to a metallicity (or dust)- luminosity correlation, or due to an increase in the dark matter fraction with luminosity. Is it possible to distinguish between these scenarios? These are the questions that this paper will attempt to answer.

We start in Section 2 with the criteria for selecting our sample of SDSS elliptical galaxies. In Section 3, we propose a mass model for these galaxies and use it to estimate dynamical masses based on measured scale sizes and velocity dispersions. We then compare stellar and dynamical mass estimates as a function of galaxy properties and discuss their implications (Sections 4 and 5). The appendix summarizes the relevant properties of the Sersic profiles we use. Wherever needed, this paper uses $(\Omega_m, \Omega_\Lambda) = (0.3, 0.7)$ and $H_0 = 70 \text{ km/s/Mpc}$.

2 THE SAMPLE

The SDSS is imaging 10^4 deg^2 of the Northern Galactic Cap in 5 bandpasses (Fukugita et al. 1996, u, g, r, i, z) using a drift scanning, mosaic CCD camera (Gunn et al. 1998) under photometric conditions (Hogg et al. 2001), and is targeting 10^6 objects for spectroscopy (Blanton et al. 2003b), most of which are galaxies with r band apparent magnitude $m_r < 17.77$ (Strauss et al. 2002). The data used in this paper cover an area of $\sim 2000 \text{ deg}^2$ and include $\sim 160,000$ galaxies with spectra, and are denoted **sample10** within the SDSS collaboration. All of these data have been reduced by highly automated photometric and spectroscopic reduction pipelines (see Stoughton et al. 2002, for details). The astrometric calibration is automatically performed by a pipeline that obtains absolute positions to better than 0.1 arcsec (Pier et al. 2003), and magnitudes are calibrated to a standard star network approximately in the AB system (Smith et al. 2002).

The SDSS pipelines return a wealth of information for all detected objects; in addition, a number of auxiliary parameters have been measured by various members of the SDSS collaboration for these objects. The principal parameters relevant to this work are mentioned below.

- Redshifts(z) and Velocity dispersions(σ): Each of the SDSS galaxy spectra is fit to a linear combination of galaxy templates at varying redshifts, broadened by a Gaussian kernel (Schlegel et al. 2003). Minimizing χ^2 over this suite of models leads to an estimate of both the redshift and the stellar velocity dispersion of the galaxy.
- Petrosian Fluxes : The primary measure of galaxy flux in the SDSS is the Petrosian magnitude, a modification of the quantity defined by Petrosian (1976); see Strauss et al. (2002) for details. Note that in the absence of seeing, the Petrosian flux is about 81.5% of the total flux of a deVaucouleurs profile. The photometric pipeline also returns the radii that enclose 50% and 90% of the Petrosian flux, $R_{p,50}$ and $R_{p,90}$ respectively, as well as the ratio of the minor to major axes, a/b , of the galaxy from model fits to a deVaucouleurs profile.
- K-corrections : All luminosities and colours used in this paper are k-corrected to the median redshift of the survey, $z_{med} = 0.1$, using the *kcorrect* package of Blanton et al. (2003a).
- Sersic Profiles : The radial intensity profiles of all of the galaxies in our sample have been fit to Sersic profiles (Sersic 1968; Blanton et al. 2002),

$$I(R) = A \exp [-(\theta/\theta_s)^{1/n}] , \quad (1)$$

where R_s is a scale radius, and n measures the concentration of the intensity profile ¹. Unlike the Petrosian magnitudes, the Sersic fits are convolved with the PSF. Therefore, the effective or half light radius of the Sersic profile, R_{50} , is a robust estimator of the galaxy size and is what we adopt throughout this paper.

- D_{4000} : The continuum break at 4000 Å, D_{4000} (Balogh et al. 1999) is one of the most prominent features in galaxy spectra, and is caused by the accumulation of a

¹ We summarize the relevant properties of the Sersic profile in the Appendix.

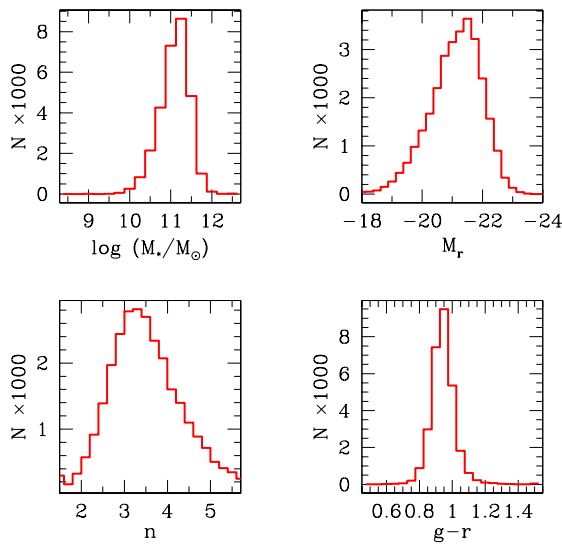


Figure 1. Properties of the sample of elliptical galaxies. The upper left panel shows the distribution of the logarithm of stellar masses, while the upper right panel is the distribution of the r -band absolute magnitudes. The lower left panel shows the Sersic indices for our sample, where $n = 4$ is the de Vaucouleurs profile, and the lower right panel is the distribution of the $g-r$ k-corrected colour.

large number of metal lines in a narrow region of the spectrum. Hot stars, indicative of a young stellar population, show a weak 4000 Å break as the principal metals causing the absorption are multiply ionized, making this feature a powerful age estimator. The strength of the break is computed following Tremonti (2002) (see also Kauffmann et al. 2003).

- Stellar masses (M_*): Kauffmann et al. (2003) compute stellar mass to light ratios for all spectroscopically observed galaxies by fitting stellar population synthesis models to the measured D_{4000} strength and the $H\delta_A$ absorption line, assuming the Kroupa (2001) initial mass function (IMF). Given this M/L ratio, the stellar mass is estimated by multiplying by the Petrosian luminosity in the z band, correcting for extinction due to dust by matching the predicted galaxy colours to the observed colours.

2.1 Selecting Ellipticals

In order to translate the velocity dispersions into dynamical mass estimates, it is important that we select galaxies that are pressure supported, and not rotationally supported. In practice, this closely corresponds to selecting a sample of elliptical galaxies. We note that our selection criteria will also allow S0's; these galaxies, although not strictly elliptical galaxies, satisfy our criterion that they have little or no rotational support. However, for simplicity, we refer to all these galaxies as elliptical galaxies. Since we desire minimal contamination from spirals, we use a combination of spectroscopic and photometric criteria, similar in spirit to those in Bernardi et al. (2003a), although differing in detail. Note

that unless specified, all the photometric quantities are measured in the r band. The cuts made were

- $D_{4000} > 1.6$: As mentioned above, a large D_{4000} corresponds to an older stellar population, normally associated with ellipticals. This particular cut is based on Kauffmann et al. (2003).
- $R_{p,90}/R_{p,50} > 2.6$ (Shimasaku et al. 2001): Elliptical galaxies have intensity profiles that are more concentrated than spirals, allowing one to separate them on the basis of a concentration parameter, $R_{p,90}/R_{p,50}$.
- No emission lines : The stellar populations of ellipticals are generally old, with little or no star formation. Since emission lines are associated with star forming regions, we reject galaxies with emission lines ($H\alpha, NII$) detected with $S/N > 3$.
- $\sigma > 70$ km/s : This cut is based on the resolution of the SDSS spectra; velocity dispersions lower than 70 km/s cannot be reliably determined.
- Minor/Major axis ratio (a/b) > 0.7 : This was chosen to eliminate large edge-on spiral galaxies that were not eliminated by the previous cuts. Also, since a large rotation velocity would tend to flatten elliptical galaxies, this eliminates galaxies with large rotation velocities.

Making these cuts reduces our sample from 165,812 to 29,469 galaxies. Fig. 1 shows some of the properties of our sample. Most of our galaxies have Sersic index n between 3 and 4 and have their Petrosian $g-r$ colour narrowly distributed around ~ 1.0 . We did not cut on either of these quantities, yet they lie in the range expected for elliptical galaxies. In addition, we have visually inspected images of a random subsample of these galaxies and have found the contamination from spirals to be less than 5 %.

3 A DYNAMICAL MODEL

In order to relate the velocity dispersions to dynamical masses, we need to develop a model of the mass distribution of the galaxy. We model each galaxy (Fig. 2, top panel) as having two spherically symmetric components, a stellar component described by a Hernquist (1990) profile,

$$\nu \propto r^{-1}(r+a)^{-3}, \quad (2)$$

and a dark matter halo. We adopt the Hernquist profile as it provides a convenient analytical approximation to the deprojected deVaucouleurs profile². Modelling the dark matter is more difficult since it involves understanding its response to the baryons. We start with an NFW profile (Navarro et al. 1997),

$$\rho \propto r^{-1}(r+r_s)^{-2}, \quad (3)$$

for the initial matter distribution, assume that a fraction F (the stellar mass fraction) condenses into stars, and that the remaining matter (the dark matter mass fraction) is adiabatically compressed by the stellar matter following

² See the Appendix for an explanation of why this is still justified for the Sersic profile fits that we use.

Blumenthal et al. (1986). Determining the final dark matter profile involves solving the equations

$$\begin{aligned} r_i M_{NFW}(r_i) &= r_f(M_*(r_f) + M_{DM}(r_f)) \\ (1 - F)M_{NFW}(r_i) &= M_{DM}(r_f) , \end{aligned} \quad (4)$$

where $M_{NFW}(r_i)$ is the initial mass profile, $M_*(r_f)$ and $M_{DM}(r_f)$ are the final stellar and dark matter profiles, and F is the stellar mass fraction. The first equation represents angular momentum conservation, while the second enforces the fact that orbits of dark matter particles do not cross. We now use the Jeans equation to find the 3D velocity dispersion profile, $\overline{v_r^2}$ (Binney & Tremaine 1987),

$$v_c^2(r) \equiv \frac{GM(r)}{r} = -\overline{v_r^2} \left(\frac{d \ln \nu}{d \ln r} + \frac{d \ln \overline{v_r^2}}{d \ln r} + 2\beta \right) , \quad (5)$$

where $M(r)$ is the total (stellar and dark) mass within r , v_c (the circular velocity) is the velocity a particle on a circular orbit would have, and β measures the anisotropy of the velocity distribution,

$$\beta = 1 - \frac{\overline{v_\theta^2}}{\overline{v_r^2}} . \quad (6)$$

While the applicability of this model to elliptical galaxies remains unclear, numerical simulations suggest it gives a good qualitative description in the region of interest ($\gtrsim 0.5R_{50}$) (M. Steinmetz, private communication). Fig. 2 (top panel) shows the initial and final integrated dark matter mass as a function of radius, as well as the stellar mass. The final circular velocity profile shown in Fig. 2 (solid line, bottom panel, the velocity was reduced by 1.65 as discussed below) is nearly flat over the range of interest, in agreement with observations of normal ellipticals (Gerhard et al. 2001). The reader is referred to Seljak (2002) for more examples and the circular velocity profiles of individual components.

We then can project this distribution to two dimensions,

$$I(R)\hat{\sigma}^2(R) = 2 \int_R^\infty \left(1 - \beta \frac{R^2}{r^2} \right) \frac{\nu \overline{v_r^2} dr}{\sqrt{r^2 - R^2}} , \quad (7)$$

where $I(R)$ is the 2D intensity distribution. The SDSS spectrograph measures the luminosity weighted average (within the fiber aperture) of the above quantity,

$$\sigma^2(R) = \frac{\int_0^R R' dR' I(R') \hat{\sigma}^2(R')}{\int_0^R R' dR' I(R')} . \quad (8)$$

Examples of velocity dispersion profiles for different values of β are shown in the lower panel of Fig. 2.

To compute the dynamical mass, we must choose a characteristic radius and relate σ at that radius to the circular velocity, v_c . The first complication is that the anisotropy β is unknown; however, as Fig. 2 suggests, the effects of β are more pronounced in the inner regions suggesting that we measure σ at large radii. This is a manifestation of the virial theorem; for an isothermal profile, the luminosity weighted velocity dispersion is simply related to the circular velocity via $v_c^2 = 3\sigma^2$. From Fig. 2, we see that $v_c(R_{50}) \approx 1.65\sigma(R_{50})$ with a scatter of $\sim 10\%$, depending of the anisotropy profile we use. This gives us a dynamical mass estimate at R_{50} ,

$$M_{dynm} = \frac{(1.65\sigma)^2 R_{50}}{G} . \quad (9)$$

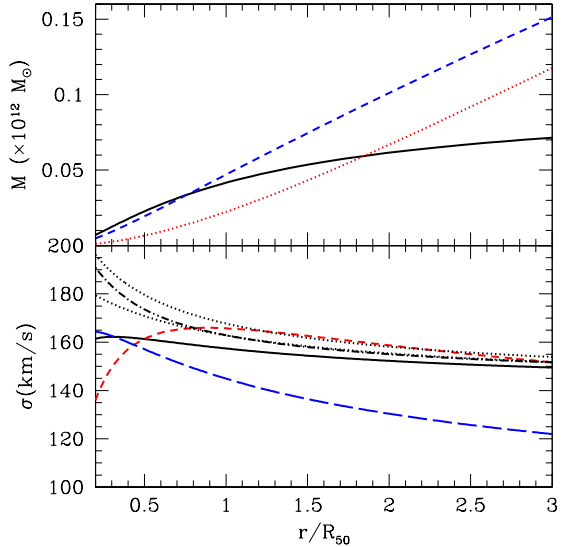


Figure 2. The upper panel shows the integrated mass of the original matter (dotted/red) profile, the stellar (solid/black) and final dark matter (dashed/blue) distributions. The lower panel is the luminosity weighted velocity dispersion profile for an isotropic $\beta = 0$ (solid), $\beta = 0.3$ (lower dotted) and $\beta = 0.5$ (upper dotted) velocity distribution. We also show a variable anisotropy profile (dot-dashed), $\beta = 4\beta_0 x/(1+x)^2$ where $x = r/r_\beta$, and $\beta_0 = 0.5$ and $r_\beta = 1.38$ kpc. The short dashed (red) line is the circular velocity profile reduced by 1.65, while the long dashed (blue) line is the profile that would be observed by a slit spectrograph (using $\beta = 0$). Both panels assumed a galaxy halo of $10^{12} M_\odot$ with a concentration (r_{virial}/r_s) of 10, and a stellar component of $10^{11} M_\odot$ with an effective radius of 5 kpc.

This dynamical mass estimate is a 3D mass, while the stellar masses are projected masses. We estimate the 3D stellar mass by considering the mass contained within the Hernquist profile at R_{50} , the projected half-light radius, which is approximately $\sim 42\%$ of the total stellar mass. Furthermore, the stellar masses are computed using the Petrosian flux, which is approximately 80% of the flux of an early type galaxy; these two factors together imply that the 3D stellar mass at R_{50} is $\sim 50\%$ of the total estimated stellar mass.

Unfortunately, the velocity dispersion estimated by the SDSS spectra is not at R_{50} , but at the fiber diameter of 3 arcseconds. One solution is to follow Bernardi et al. (2003a) and apply an empirical correction to the measured dispersion. Another approach, also suggested there, is to stack galaxies of similar masses and physical sizes and construct a velocity dispersion profile. These galaxies are at a range of redshifts, so the 3 arcsecond fibers probe the velocity dispersion at different physical radii, allowing us to construct a composite velocity profile. We can then use this profile to correct the measured velocity dispersions out to R_{50} .

However, naively making subsamples is dangerous because the SDSS spectroscopic sample is magnitude limited, i.e. to a good approximation, it included all galaxies with $m_r < 17.77$. This implies that galaxies at higher redshifts are more luminous on average, which could introduce spurious correlations between observed quantities. Therefore, to ensure uniformity, all the subsamples we construct in this pa-

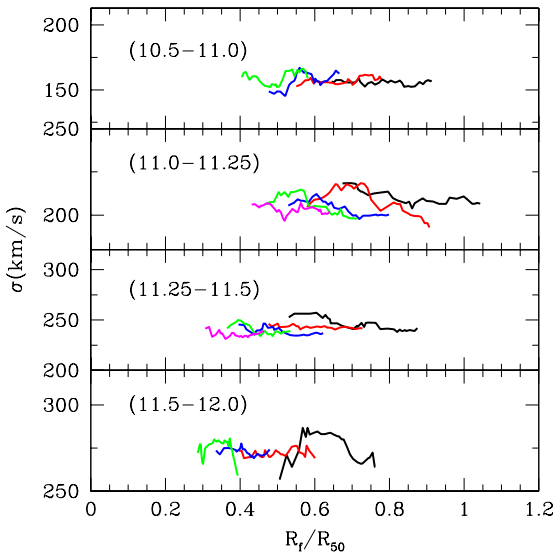


Figure 3. Estimated velocity profiles for our sample of ellipticals in SDSS as a function of R_f/R_{50} where R_f is the fiber radius of 1.5 arcseconds. The different panels are different stellar mass volume limited subsamples, where the panels are labelled by the logarithm of the stellar mass range. The different line segments in each panel show the median velocity dispersion of subsamples in the physical size of the galaxy. Note that the size of the galaxy increases from right to left. The various size ranges considered are (from top to bottom) 2.5-6.0, 3.0-6.0, 4.0-10.0 and 5.0-13.0 kpc. The volume limited subsamples ensure a uniform sample over the redshift range of interest. The velocity profiles derived here are consistent with being flat over the region of interest.

per are volume limited, including only those galaxies which would remain in the sample at the redshift limits.

Fig. 3 shows the velocity profiles estimated by stacking galaxies. The different panels are different volume limited mass samples that uniformly sample the redshift range, while the different line segments are the median velocity dispersions of subsamples of similar physical sizes. The profiles are consistent with being flat. This would appear inconsistent with the velocity dispersion profiles measured from individual ellipticals which, in general, decline with radius (e.g. Kronawitter et al. 2000). However, the profiles are significantly flatter when luminosity weighted within the fiber, shown in Fig. 2 comparing the profile that would be seen through a slit with that through a fiber. We therefore use the velocity dispersion measured through the 3 arcsecond aperture as the dispersion at R_{50} . While the statistical velocity dispersion profiles are in a good agreement with the isotropic model predictions, the narrow dynamic range of volume limited subsamples prevents us from making any strong conclusions on the anisotropy parameter β .

4 RESULTS

Now that we have both stellar and dynamical masses, we can compare them. Figs. 4 and 5 show the stellar and dynamical mass to light ratios respectively as a function of luminosity. A useful consistency test of both the stellar and dynamical masses is that M_{dynm}/L ($\sim 5 - 8$) is greater than M_*/L

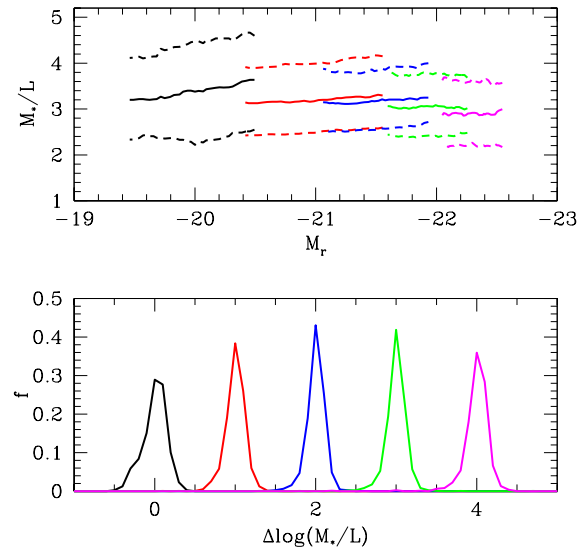


Figure 4. The upper panel is the stellar mass to light ratio (M_*/L) as a function of r band luminosity. The different segments/colours correspond (from left to right) to volume limited subsamples within redshift intervals 0.04-0.08 (black), 0.08-0.12 (red), 0.12-0.16 (blue), 0.16-0.20 (green), 0.20-0.24 (magenta). The solid line is the median of the distribution, while the lower and upper dashed lines are the 16% and 84% intervals. The lower panel shows the distribution of M_*/L at the median luminosity of each redshift subsample, staggered by $\Delta \log(M_*/L) = 1$ for clarity.

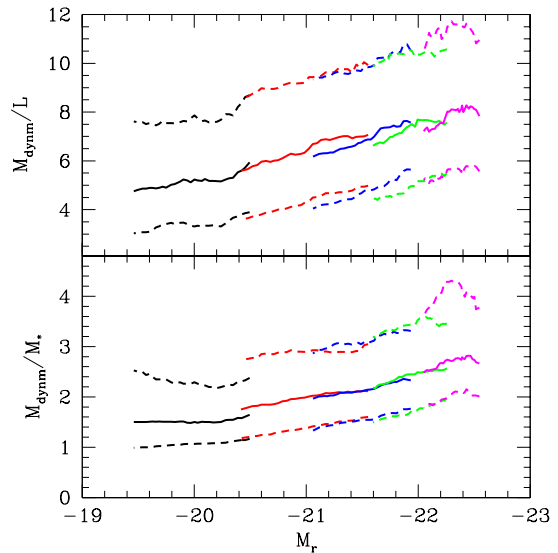


Figure 5. Same as Fig. 4 except that the dynamical mass to light (M_{dynm}/L) and the dynamical mass to stellar mass ratio (M_{dynm}/M_*) are plotted. Although we don't show it explicitly here, the scatter is consistent with log-normal.

(~ 3). Since the stellar masses are sensitive to the choice of IMF, this constrains the possible IMF's as we discuss in the next section. Also, M_{dynm}/L increases roughly as $L^{0.17}$, while M_*/L is constant, or slightly decreasing. The apparent decrease in M_*/L with luminosity could be interpreted as luminosity evolution, although the statistical significance of the decrease is unclear (see below). Note that the scatter in both quantities is consistent with being log-normal, with a width of $\sim 30\%$ for the stellar masses and slightly more for the dynamical masses.

A relevant question is whether this scatter is due to measurement error or an intrinsic scatter in galaxy properties. The errors in the stellar masses are obtained by integrating over a grid of population synthesis models to obtain the 16% and 84% confidence intervals; these errors are $\sim 25\%$. Estimating an error for the dynamical mass is more involved; we assume a 10% error on the conversion of σ to the circular velocity (see Fig. 2 for a justification) and a further $\sim 10\%$ error on the measurement of $\sigma^2 R_{50}$. This yields an error in the dynamical mass of $\sim 30\%$. This implies that the dominant source of scatter is measurement errors, so it is possible that the intrinsic correlations are tighter than what is observed.

The measurement errors can be dominated by systematic or statistical errors. Systematic errors can be caused by the velocity dispersion-mass conversion we have assumed, errors in extrapolation to R_{50} , or by errors in the stellar mass determination. Pure statistical errors, such as those from measurement errors, will average out in median quantities. If statistical errors dominate, then the trends in the medians of these distributions are highly statistically significant. If the errors are dominated by systematics, the trends may still be significant, as long as the systematic error does not couple to the parameter that is varied. In all our figures, we have presented the average 1σ contours for individual objects. This is the most conservative error estimate and it should be kept in mind that the errors on median quantities may be significantly smaller than this.

However, there are possible uncertainties in the stellar mass estimations that could lead to systematic errors. The stellar masses are estimated by comparing the measured D_{4000} and $H\delta_A$ indices with detailed stellar population synthesis models. In order to estimate the robustness of the masses to these details, we compared the stellar masses used here with those computed by Panter et al. (2002) and found that, for the subsample of ellipticals found in both catalogs, the differences were consistent with the errors. Specifically, all the trends found in this paper are also present for the stellar masses estimated by Panter et al. (2002).

Another potential source of systematic error is colour gradients: M_*/L is determined from the spectra within the fiber, typically at $0.4\text{--}0.8R_{50}$, and then assumed to hold within R_{50} . We can try to measure an average M_*/L profile using the same method we used to estimate the velocity dispersion profile. This is shown in Fig. 6; as before, the different panels are different stellar mass ranges, while the different line segments are the median M_*/L for galaxies of similar physical sizes. There is a modest trend towards decreasing M_*/L with radius, although the statistical significance is unclear. If we attribute the observed trends to a colour gradient, our stellar masses are only upper limits on the true stellar mass. The suggested trends would reduce the

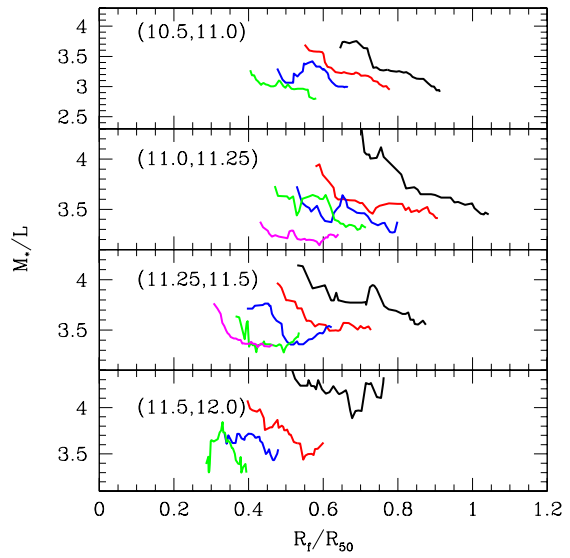


Figure 6. M_*/L profiles for our sample, analogous to Fig. 3. The mass subsamples are labelled in each panel, while the individual lines are medians for different physical sizes.

stellar mass by at most 20%. While this would alter the precise form of the correlations that we have observed, it would increase the dark matter fraction observed, but would not change any of the trends we find. However, luminosity evolution would also cause a similar trend and is difficult to disentangle from M_*/L gradients. Therefore, we choose to be conservative and assume that the estimated M_*/L value is applicable at R_{50} . As a final check on systematics, we find that our trends remain unchanged even if we select only very spherical objects with $a/b > 0.9$ that are unlikely to show any rotation. This provides additional support to our assumption of ignoring rotation in the analysis.

We can now consider galaxies of a given luminosity and ask if there is any variation in M_{dynm}/M_* as a function of the size of the galaxy. In order to do this, we start with the volume limited samples discussed above and construct luminosity subsamples 0.5 magnitudes in width, centred about the median luminosity of each original sample. Fig. 7 shows M_{dynm}/M_* as a function of R_{50} , for samples created in this manner. The ratio of dynamical mass to stellar mass increases roughly linearly with radius, with a slope of ~ 0.14 . Fig. 8 shows the same relation for stellar and dynamical mass subsamples; the relations for these subsamples are very similar to those for luminosity.

It is interesting to ask whether these correlations can be explained with the model of Section 3. The model has four parameters, the virial mass and scale size of the halo, and the stellar mass and scale size of the galaxy. The latter two of these are directly constrained by observations. We parametrise the scale size of the halo (Eq. 3) by the concentration parameter, $c \equiv r_{vir}/r_s$, where the virial radius, r_{vir} , is determined by the virial mass,

$$M_{vir} = \frac{4\pi}{3} \Delta \rho_{crit} r_{vir}^3, \quad (10)$$

where $\Delta (= 200)$ is the spherical overdensity and ρ_{crit} is the critical density. While numerical simulations suggest that

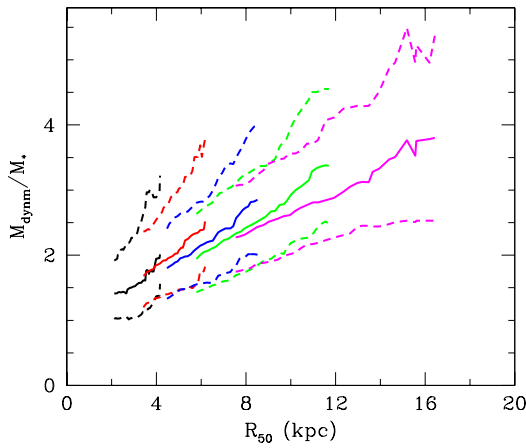


Figure 7. M_{dynam}/M_* as a function of the physical size (half light radius) of the galaxy. The different segments/colours correspond to cutting the sample in redshift as in Fig. 4, and then selecting a narrow luminosity bin around the median luminosity of the redshift subsample. The median luminosities for the subsamples are (from left to right) are -19.93, -20.78, -21.30, -21.78 and -22.20.

the concentration decreases with virial mass, this variation is small over the range considered here. We thus make the assumption that the concentration is constant ($c = 12.7$) independent of the size of the halo. This leaves us with only the virial mass of the halo to vary; Fig. 9 compares the prediction of this model for the dynamical to stellar mass ratio as a function of R_{50} with the observed result, for galaxies with stellar masses $\sim 1.5 \times 10^{11} M_\odot$. The model does well predicting the general trend for this and other stellar masses, although the slopes are shallower than what is observed. While the statistical significance of the discrepancy is small, it is possible that it is caused by the restrictive assumptions of the model. Allowing either the concentration or virial mass to vary with the size of the galaxy of a given stellar mass can reproduce the observed slope.

This simple one-parameter family of models provides a novel method of estimating the virial mass of the halo in which a galaxy of a given stellar mass resides. This method is demonstrated in Fig. 9; one adjusts the virial mass to best match the observed correlation of M_{dynam}/M_* with R_{50} , while ‘‘errors’’ can be estimated by matching to the 16% and 84% contours. The results of this exercise are in Fig. 10 as a function of stellar mass. Here again we take the conservative approach of assuming the errors to be dominated by systematics. If the errors are statistical, then the usual $1/\sqrt{N}$ factor can be applied and the errors on the mean relation become considerably smaller. This figure argues that the virial masses of halos are 10 times the stellar mass of ellipticals at the high mass end and somewhat less at the lower mass end.

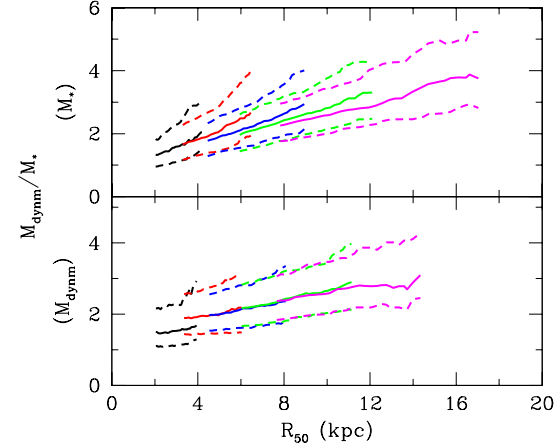


Figure 8. Same as Fig. 7 except that the subsample is cut in stellar (upper panel) and dynamical (lower panel) mass. From left to right, the median stellar masses are $4.36, 9.33, 15.3, 22.8$ and $31.8 \times 10^{10} M_\odot$, while the median dynamical masses are $3.57, 9.51, 16.5, 27.1, 42.2 \times 10^{10} M_\odot$.

5 DISCUSSION

In this paper, we have compared stellar and dynamical mass estimates for a sample of elliptical galaxies in the SDSS, and studied the dependence of that relation on the luminosity and size of the galaxy.

The first conclusion that we draw from this work is that stellar mass estimates are consistent with the dynamical estimates, i.e. $M_* \leq M_{dynam}$ with $M_* \sim M_{dynam}$ for high surface brightness (low R_{50}) galaxies. This is far from a trivial conclusion, since the procedure to estimate stellar masses is a rather involved one. In particular, the stellar masses are extremely sensitive to the stellar initial mass function. Here we have followed Kauffmann et al. (2003) and adopt the Kroupa (2001) IMF; replacing it with a Salpeter IMF increases the number of low-mass stars, effectively increasing all the inferred stellar masses. An examination of Fig. 7 shows that the stellar masses would no longer be consistent with the dynamical estimates in that case for high surface brightness (low R_{50}) galaxies. This statement depends on how one regularises the divergence of the Salpeter IMF at low masses, and therefore, must only be interpreted as a constraint on the minimum mass that the Salpeter slope can extend to. Our results suggest that a cutoff at $M > 0.1 M_\odot$ is required, consistent with IMF measurements from young embedded clusters (Muñch et al. 2002).

In what follows, we assume that the difference between the dynamical and stellar masses is due to the presence of a dark matter component of the galaxies. Ellipticals often have a hot gas component; however, it is a relatively minor contribution to the mass (Sarazin 1997), and the stellar mass is, to a good approximation, the baryonic mass of the galaxy.

Given that approximation, we can draw the following conclusions about elliptical galaxies in SDSS :

- The fraction of dark matter increases with increasing

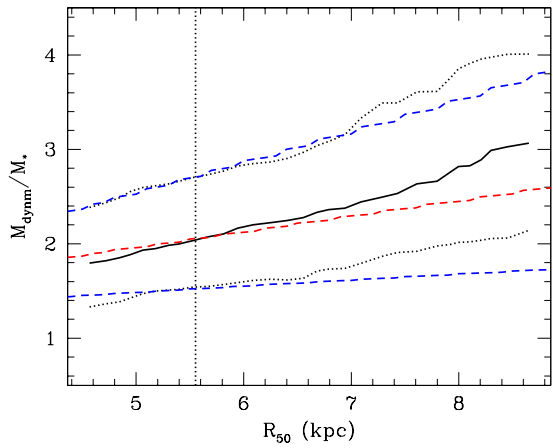


Figure 9. The solid and dotted lines show the median and 16% and 84% contours of the distribution of M_{dynam}/M_* as a function of R_{50} for a volume limited subsample with stellar mass between 1.17 and $1.86 \times 10^{11} M_\odot$ (median value of $1.5 \times 10^{11} M_\odot$). The central dashed line shows the prediction of the model in Sec.3 for the median stellar mass and a halo mass of $1.35 \times 10^{12} M_\odot$, while the upper and lower lines have halo masses of $6.0 \times 10^{11} M_\odot$ (lower) and $4.8 \times 10^{12} M_\odot$. All the initial halos had concentration parameters $c = 12.7$. The vertical dotted line is the median size of all the galaxies in the sample.

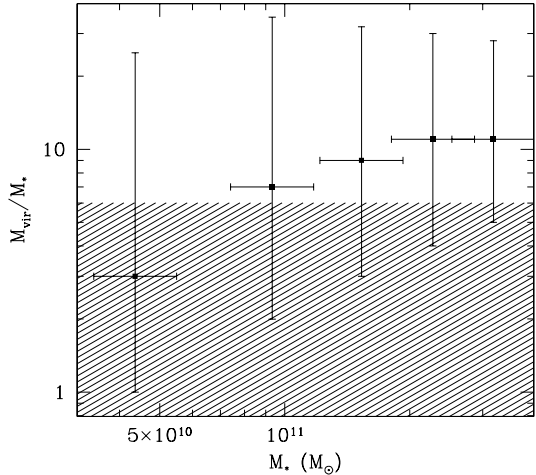


Figure 10. The ratio of the virial mass to stellar mass as a function of stellar mass calculated using the methods described in the text and Fig.9. The shaded region is excluded by the cosmic baryonic fraction of $\sim 17\%$ measured by WMAP, assuming only baryons within the virial radius can cool and form stars.

luminosity: As is evident from Figs.4 and 5, the stellar mass to light ratio is approximately independent of luminosity, while $M_{dynam}/L \propto L^{0.17}$, implying an increasing dark matter fraction with luminosity. Note also that the dependence of M_{dynam}/L on L is consistent with the results of Bernardi et al. (2003b), $M_{dynam}/L \propto L^{0.14 \pm 0.02}$.

This result suggests that the tilt in the fundamental plane is caused by an increasing dark matter fraction with luminosity. Recall that the virial prediction for the fundamental plane,

$$\sigma^2 \propto \left(\frac{M}{L}\right) R \left(\frac{L}{R^2}\right) \propto RI, \quad (11)$$

is traditionally modified by assuming that the mass to light ratio varies with luminosity, $(M/L) \propto L^\alpha$. As discussed in the introduction, there are two possibilities to explain this scaling, variations in metallicity or in the dark matter fraction. Variations in metallicity would show up as variations in M_*/L , while variations in the dark matter fraction would be evident in M_{dynam}/L . We observe that M_*/L is approximately independent of L , while M_{dynam}/L increases with L , favouring the conclusion that the tilt is due to dark matter and not metallicity. This is the opposite conclusion from that reached by Gerhard et al. (2001) who argue that a maximal stellar mass is supported by population synthesis models, and therefore, one need not invoke dark matter. Our approach is different; we use stellar masses estimated independently of the dynamical estimates. Comparing these shows that elliptical galaxies have a significant dark matter component within an effective radius, with as much as 3-4 times the stellar component for the largest galaxies.

We can also compare our results with those of Borriello et al. (2003), which attempted to fit the fundamental plane with stellar and dark matter models similar to those we use. However, Borriello et al. (2003) leave the stellar mass to light ratio a free parameter; this leads them to conclude that the data favours a model with no dark matter and $M_*/L \sim 5.3$. This is approximately a factor of 2 greater than our estimates of $M_*/L \sim 3$; moreover, we argue that changing our IMF to agree with the higher M_*/L would make the stellar masses inconsistent with our dynamical estimates for high surface brightness galaxies.

- The dark matter fraction increases with increasing size at constant luminosity (Fig. 7). Note that this is a robust result, since similar trends are also seen if the stellar mass or velocity dispersion are kept constant, instead of the luminosity (Fig.8). For the highest surface brightness galaxies, the stellar mass approaches the dynamical mass. This suggests that the IMF based on local observations is also applicable to ellipticals. A simple model of a galaxy embedded in a dark matter halo with a constant star formation efficiency ³ captures the qualitative trends. In such a model a low surface brightness galaxy and a high surface brightness galaxy of equal luminosity sit in equal dark matter halos, but the low surface brightness galaxy is more spread out, so the ratio of stellar to dark matter mass is lower. These trends are thus expected in ab-initio models of galaxy formation. To explain them without the dark matter would require introducing an IMF that depends on the surface brightness.

³ In other words, that the stellar mass fraction, F , is independent of the size of the galaxy.

While this model can explain most, if not all, of the trends suggested by the observed relations, one question remains: what sets the scale size of the galaxy? As Fig. 7 shows, the half light radius varies by a factor of two at any given luminosity. One simple possibility is that it is related to the scale radius of dark matter, which simulations suggest has a considerable scatter (Bullock et al. 2001). However, if a more compact galaxy is in a more concentrated dark matter halo then this would make the agreement in Fig. 9 worse, since that figure suggests we need less dark matter in compact galaxies and more in low surface brightness galaxies. In this case the assumption of star formation efficiency being independent of galaxy scale size must also be violated. While we do not have definitive answers to these questions, we note that ongoing galaxy-galaxy lensing studies on the same SDSS sample may be able to provide useful additional information, since it can determine the virial mass as a function of luminosity, surface brightness etc.

We also use this model to estimate the virial mass as a function of mass and luminosity for our sample of galaxies. Although the errorbars are large, we find that the virial mass of the halo is around 10 times the stellar mass of the galaxy (Fig. 10). We note that our modelling assumes that halos are undisturbed. Many of the ellipticals are in denser environments of groups and clusters. If the galaxy is at the center of the group then our modelling still applies. If it is a satellite then some of the dark matter attached to the galaxy before it merged into the group halo was likely stripped off due to the tidal effects. In this case our estimates apply to the virial mass of the galaxy prior to merging. This is the mass of interest if most of the stellar mass has been assembled prior to the galaxy merging into the group or cluster.

Comparing 10% stellar mass fraction to the cosmic baryonic fraction of 17% from WMAP (Spergel et al. 2003) implies that 60% of the initial gas has been converted to stars; a 1σ uncertainty takes us between 25% and 100%. This is not necessarily inconsistent with the global stellar mass fraction, which is only around 5-10% of baryons (Balogh et al. 2001; Dickinson et al. 2003): it suggests that the efficiency of star formation peaks at $M_{\text{vir}} \sim 10^{12} M_{\odot}$ and is likely to be much smaller in either lower and higher mass halos. We observe this trend at the high mass end, where the dark matter fraction increases with increasing mass, although the uncertainties in our measurement are large. The implication of an increasing dark matter fraction with luminosity is that the star formation is suppressed in the most massive halos, as expected for example by the longer cooling times in hotter halos. The sample of low mass ellipticals is too small to observe the reverse trend at the low mass end. Both the absolute value of the star formation efficiency and its trend with luminosity/stellar mass are in agreement with galaxy-galaxy lensing results, which provide an independent estimate of the total mass of the halo (Guzik & Seljak 2002). These additional constraints on the mass also allow for a more detailed modelling of the structure of ellipticals. Ultimately, we hope that these results will both inform and constrain theories of galaxy formation.

We would like to thank Daniel Eisenstein, David Hogg, Raul Jimenez, Yeong-Shang Loh and Scott Tremaine for useful discussions. U.S. acknowledges support from the Packard

and Sloan foundations and NSF CAREER-0132953. M.A.S. acknowledges support of NSF grant AST-0071091.

Funding for the creation and distribution of the SDSS Archive has been provided by the Alfred P. Sloan Foundation, the Participating Institutions, the National Aeronautics and Space Administration, the National Science Foundation, the U.S. Department of Energy, the Japanese Monbukagakusho, and the Max Planck Society. The SDSS Web site is <http://www.sdss.org/>.

The SDSS is managed by the Astrophysical Research Consortium (ARC) for the Participating Institutions. The Participating Institutions are The University of Chicago, Fermilab, the Institute for Advanced Study, the Japan Participation Group, The Johns Hopkins University, Los Alamos National Laboratory, the Max-Planck-Institute for Astronomy (MPIA), the Max-Planck-Institute for Astrophysics (MPA), New Mexico State University, University of Pittsburgh, Princeton University, the United States Naval Observatory, and the University of Washington.

APPENDIX A: PROPERTIES OF SERSIC PROFILES

The Sersic profile is an obvious generalisation of the classification of galaxies into deVaucouleurs and exponential intensity profiles,

$$I(R) \propto \exp(-x^{1/n}), \quad (A1)$$

where x is a dimensionless radial variable, R/R_s . Exponential and deVaucouleurs profiles correspond to $n = 1$ and $n = 4$ respectively; in general, the Sersic index n can be any positive real number. Below, we summarise the relevant properties of Sersic profiles; a more detailed discussion is contained in Ciotti (1991) and references therein.

The first quantity of interest is the half light radius R_{50} . Defining $y \equiv x^{1/n}$, we can solve for the integrated intensity profile,

$$L(R) \propto \int_0^y dy' y'^{2n-1} \exp(-y') \propto \gamma(2n, y), \quad (A2)$$

where $\gamma(m, y)$ is the incomplete Gamma function. Using the above result, we see that R_{50} can be determined by solving,

$$\frac{\gamma(2n, b(n))}{\Gamma(2n)} = \frac{1}{2}, \quad (A3)$$

where $\Gamma(2n) \equiv \gamma(2n, \infty)$ is the Gamma function and $b(n) = (R_{50}/R_s)^{1/n}$. This equation can be solved numerically, but a useful approximation is $b(n) = 2n - 0.324$.

We can also solve for the deprojected Sersic profile $\nu(r)$; this is obtained via the Abel transform,

$$\nu(r) = -\frac{1}{\pi} \int_r^\infty \frac{dI}{dR} \frac{dR}{\sqrt{R^2 - r^2}}. \quad (A4)$$

In order to quantify the differences between the different values of n , it is useful to consider the total mass/light contained within a radius r . This is shown in Fig. A1 where we have scaled all the radii by R_{50} . Note that the discrepancies between different values of n are marginal, especially at radii greater than $0.3R_{50}$ (which contains less than 20% of

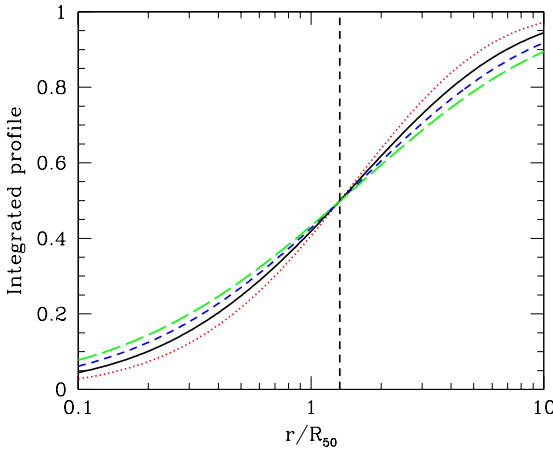


Figure A1. Integrated light profiles for deprojected Sersic profiles for $n=3$ [dotted, red], 4 [solid, black], 5 [short-dashed, blue], 6 [long-dashed, green] profiles, as a function of r/R_{50} where R_{50} is the projected half-light radius. The vertical dashed line marks the 3D half light radius for the $n=4$ profile.

the total mass/light). This justifies our modelling the stellar light distribution of all galaxies with a Hernquist profile, even when $n \neq 4$.

REFERENCES

Balogh M. L., Morris S. L., Yee H. K. C., Carlberg R. G., Ellingson E., 1999, *ApJ*, 527, 54

Balogh M. L., Pearce F. R., Bower R. G., Kay S. T., 2001, *MNRAS*, 326, 1228

Bernardi M., Sheth R. K., Annis J., Burles S., et al., 2003a, *AJ*, 125, 1817

Bernardi M., Sheth R. K., Annis J., Burles S., et al., 2003b, *AJ*, 125, 1849

Bernardi M., Sheth R. K., Annis J., Burles S., et al., 2003c, *AJ*, 125, 1866

Bernardi M., Sheth R. K., Annis J., Burles S., et al., 2003d, *AJ*, 125, 1882

Binney J., Tremaine S., 1987, *Galactic Dynamics*. Princeton, NJ, Princeton University Press, 1987

Blanton M. R., Brinkmann J., Csabai I., Doi M., et al., 2003a, *AJ*, 125, 2348

Blanton M. R., Hogg D. W., Bahcall N. A., et al., 2002, *ApJ*. in press (astro-ph/0209479)

Blanton M. R., Lin H., Lupton R. H., Maley F. M., Young N., Zehavi I., Loveday J., 2003b, *AJ*, 125, 2276

Blumenthal G. R., Faber S. M., Flores R., Primack J. R., 1986, *ApJ*, 301, 27

Borriello A., Salucci P., Danese L., 2003, *MNRAS*, 341, 1109

Bullock J. S., Kolatt T. S., Sigad Y., Somerville R. S., Kravtsov A. V., Klypin A. A., Primack J. R., Dekel A., 2001, *MNRAS*, 321, 559

Ciotti L., 1991, *A&A*, 249, 99

de Vaucouleurs G., 1948, *Annales d'Astrophysique*, 11, 247

de Zeeuw P. T., Bureau M., Emsellem E., Bacon R., et al., 2002, *MNRAS*, 329, 513

Dickinson M., Papovich C., Ferguson H. C., Budavári T., 2003, *ApJ*, 587, 25

Djorgovski S., Davis M., 1987, *ApJ*, 313, 59

Dressler A., Lynden-Bell D., Burstein D., et al., 1987, *ApJ*, 313, 42

Faber S. M., Jackson R. E., 1976, *ApJ*, 204, 668

Fukugita M., Ichikawa T., Gunn J. E., Doi M., Shimasaku K., Schneider D. P., 1996, *AJ*, 111, 1748

Gerhard O., Kronawitter A., Saglia R. P., Bender R., 2001, *AJ*, 121, 1936

Gunn J. E., Carr M., Rockosi C., Sekiguchi M., et al., 1998, *AJ*, 116, 3040

Guzik J., Seljak U., 2002, *MNRAS*, 335, 311

Hernquist L., 1990, *ApJ*, 356, 359

Hogg D. W., Finkbeiner D. P., Schlegel D. J., Gunn J. E., 2001, *AJ*, 122

Kauffmann G., Heckman T. M., White S. D. M., et al., 2003, *MNRAS*, 341, 33

Koopmans L. V. E., Treu T., 2003, *ApJ*, 583, 606

Kronawitter A., Saglia R. P., Gerhard O., Bender R., 2000, *A&AS*, 144, 53

Kroupa P., 2001, *MNRAS*, 322, 231

McKay T. A. et al., 2001, *ApJ*. submitted (astro-ph/0108013)

Muench A. A., Lada E. A., Lada C. J., Alves J., 2002, *ApJ*, 573, 366

Navarro J. F., Frenk C. S., White S. D. M., 1997, *ApJ*, 490, 493

Panter B., Heavens A. F., Jimenez R., 2002, *MNRAS* submitted (astro-ph/0211546)

Petrosian V., 1976, *ApJ*, 209, L1

Pier J. R., Munn J. A., Hindsley R. B., Hennessy G. S., Kent S. M., Lupton R. H., Ivezić Ž., 2003, *AJ*, 125, 1559

Sarazin C. L., 1997, in *ASP Conf. Ser.* 116: The Nature of Elliptical Galaxies; 2nd Stromlo Symposium, p. 375, ed. M. Arnaboldi; G. S. Da Costa; and P. Saha

Schlegel D. J., et al., 2003, in preparation

Seljak U., 2002, *MNRAS*, 334, 797

Sersic J. L., 1968, in *Atlas de Galaxies Australes*

Shimasaku K., Fukugita M., Doi M., Hamabe M., et al., 2001, *AJ*, 122, 1238

Smith J. A., Tucker D. L., Kent S., Richmond M. W., et al., 2002, *AJ*, 123, 2121

Spergel D. N., Verde L., Peiris H. V., Komatsu E., et al., 2003, *ApJ*. in press (astro-ph/0302209)

Stoughton C., Lupton R. H., Bernardi M., Blanton M. R., et al., 2002, *AJ*, 123, 485

Strauss M. A., Weinberg D. H., Lupton R. H., et al., 2002, *AJ*, 124, 1810

Tremonti C. A., 2002, Ph.D. thesis, Johns Hopkins Univ.

Tully R. B., Fisher J. R., 1977, *A&A*, 54, 661

York D. G. et al., 2000, *AJ*, 120, 1579